Article

Molecular Dynamics Simulations of a Catalytic Multivalent Peptide–Nanoparticle Complex

Sutapa Dutta [1,2], Stefano Corni [1,2,*] and Giorgia Brancolini [2,*]

[1] Dipartimento di Scienze Chimiche, Università di Padova, 35131 Padova, Italy; sutapa.dutta@unipd.it
[2] Istituto Nanoscienze, CNR-NANO S3, via G. Campi 213/A, 41125 Modena, Italy
* Correspondence: stefano.corni@unipd.it (S.C.); giorgia.brancolini@nano.cnr.it (G.B.);
  Tel.: +39-049-8275295 (S.C.); +39-059-2055333 (G.B.)

Abstract: Molecular modeling of a supramolecular catalytic system is conducted resulting from the assembling between a small peptide and the surface of cationic self-assembled monolayers on gold nanoparticles, through a multiscale iterative approach including atomistic force field development, flexible docking with Brownian Dynamics and μs-long Molecular Dynamics simulations. Self-assembly is a prerequisite for the catalysis, since the catalytic peptides do not display any activity in the absence of the gold nanocluster. Atomistic simulations reveal details of the association dynamics as regulated by defined conformational changes of the peptide due to peptide length and sequence. Our results show the importance of a rational design of the peptide to enhance the catalytic activity of peptide–nanoparticle conjugates and present a viable computational approach toward the design of enzyme mimics having a complex structure–function relationship, for technological and nanomedical applications.

Keywords: molecular dynamics; multiscale modeling; nanozymes; functionalized metal nanoparticles; peptide

1. Introduction

Nanozymes [1–8], the artificially engineered functional nanomaterials, exhibit natural enzyme like intriguing catalytic activity and thus have huge applications in disease diagnosis [4–6,9], nanomedicine [4–6,10], environmental treatment [4], antimicrobial agent [11]. Although the existing natural enzymes demonstrate a potential role in medicine and industry, their functions are often sensitive to high temperature and extreme pH; moreover, high-cost preparation, difficulty in recycling, substrate sensitivity, low operational stability are some obstacles [1,3–7] that hinder their performance. Thus, the era of synthetic enzymes has been encompassing a broad range of scientific research studies; in particular, using polymers, dendrimers, fullerenes, micelles, and nanomaterials, to name a few [4,5,7]. Among them, gold nanoclusters [12–15] (diameter < 10 nm) are emphasized as an impressive strategy not only because of the inherent optic, electronic, magnetic properties, but also for their easy surface modification, biocompatibility, inertness, low cost; leading to enhanced durability, stability and catalytic activity of nanozymes. In particular [12–15], gold monolayer protected clusters (Au-MPC), the nanoclusters passivated by self-assembled monolayer of functional thiol mimicking enzymatic complexity along with the functional environment, have manifested exceptional catalytic activity due to multi-valency and cooperative binding.

In this paradigm, usage of short peptide sequence [16–21] to adhere on self-assembled thiolated-ligands over the surface of nanocluster or to form self-assembly of cysteine containing peptides over gold cluster as a scaffold to develop minimalist biocatalyst is one of the recently developed design techniques both from theory and experimental perspectives [16–21]. As to theoretical studies, important efforts have been directed towards the development of novel Force Field (FF) parameters to correctly describe peptide-capped

gold nanoparticles (NP) by means of atomistic simulations. From simulations, observed experimental evidences have been interpreted as the result of changes in peptide conformation due to the gold nanocluster [22], or to the presence of water molecules and structured sulphur interfacial atoms within the peptide monolayer [23], or the protonation/deprotonation state of peptide-capped gold functional groups [24]. It also has been shown that the self-assembly of bio-functionalized gold NPs [25] can be affected by the flexibility, stability and conjugation dynamics of the peptide functional groups which, in turn, is a function of the peptide length. The role of curvature and ligand properties on the hydrophobicity of small gold NPs as well as larger gold NPs (e.g., modeled as planar gold SAMs), has been systematically investigated by atomistic simulations [26–28]. Similarly, the role of polymer chain lengths in polymer-capped silver nanoparticles [29,30] has been addressed by means of fully atomistic Molecular Dynamics (MD) simulations. In addition, the role of protonation of side chain arginine moieties on the adsorption of poly-arginine to silver NP as a function of pH has been investigated computationally [31]. Details of the interaction between amyloid β fibrils gold nanoparticles functionalized with ligands with different terminal groups [32–34] have been disclosed through MD simulation. Multiscale MD simulations [35,36] have been applied to unravel protein conformation and driving forces in protein–corona complexes formation. Similarly, coarse-grained MD simulations [37–39] of plasma proteins interacting with gold nanoparticles have revealed mutual competition among binding affinities, protein concentration dependent adsorption, effects of orientation on induced conformational changes of proteins upon adsorption on NPs. In a recent experimental work [40], the role of peptide topology on the catalytic activity of peptide-NP conjugates has been studied and an approach toward the design of enzyme mimics has been proposed. However, despite many works done in the field, the rational design of enzyme mimics with enhanced catalytic activity still remains largely elusive.

In this work, we perform fully atomistic MD simulations of two peptides of different length, H_1 (seq: HWDDD) and H_3 (seq: HHHWDDD) interacting with Au-MPC, namely $Au_{144}(L)_{60}(L = S(CH_2)_8NH_2^+)$. The supramolecular system was prepared and characterized experimentally [41] through the self-assembly of the small peptides on the surface of Au-MPCs. Self-assembly is required for the catalysis, since the peptides do not display any catalytic activity in the absence of Au-MPCs. The peptide was chosen to contain three aspartic acid residues (D) at the C-terminal tail to bind to the positively charged surface of Au-MPC (1.8 ± 0.3 nm), one Tryptophan (W) to be used as a fluorescent probe and a different number of Histidine (H_1 or H_3 affecting the peptide length) at the N-terminal tail, which are responsible for the catalytic activity. Experimentally, a linear correlation was noticed between the increase in the catalytic rate constant and the number of Histidine present in the sequence (H_{1-3}) [41], suggesting the importance of peptide sequence length in modulating catalytic activity of this kind of multivalent system. We investigated this system using atomistic simulations. Molecular simulations can provide an atomistic insight into the interactions between peptides and the surface of Au-MPC, revealing details that cannot be accessed easily through experiments. In particular, quantities such as the spatio-temporal aspects of interactions involved between peptide-Au-MPC, the conformational changes of the peptide induced by the environment and the diffusion dynamics of the peptide over the surface of Au-MPCs can be accessed by atomistic simulations.

The next section reports the details of the used methods. A section of results illustration follows. Conclusions and perspective are finally illustrated.

2. Results

2.1. MD of Free Peptide and Free Au-MPC in Water

2.1.1. MD of Peptide in Water

RMSD is computed with respect to peptide backbone atoms as well with respect to C_α atom of the entire peptide, as a function of simulation time; results are shown in Figure S1d,e.

Cluster analysis is performed on trajectories of peptide H_1 generated over the last 500 ns data: the most populated cluster accounts for 19,456 structures (RMSD cut-off 0.1 nm) and it is showing an elongated conformation of H_1 (Figure 1a), this conformation being very similar to that obtained after homology modeling (Figure S1a). The other two consecutive clusters are present (Figure 1a), having 13,310 and 5261 structures each, in which the H_1 peptide adopts a "horse shoe shaped" and a new stretched conformation (with a different orientation of terminal residues), respectively. The transition between the first two most probable conformations of this peptide occurs ~10 ps scale, whereas the second one sustains for a smaller time interval ~10–20 ns span continuously in different time windows over the entire simulation period, the first conformation persists consistently for ~100 ns time scale in various time windows. Thus, the peptide in horse-shoe-shaped conformation is not stable over a larger time interval. In the case of H_3, the two most popular and comparatively different conformations are found, both with the peptide in a stretched conformation with slightly different bending at C terminal as shown by RMSD 2.2 Å (~10,000 and ~7000 number of structures respectively), as shown in Figure 2a.
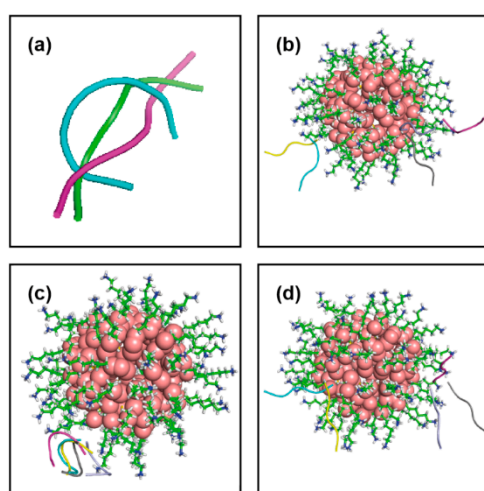

Figure 1. (**a**) Three different conformations of shorter peptide, H_1. (**b**) Different docking poses obtained for first conformation of H_1 with $Au_{144}(L)_{60}$, gold: sphere, functionalized ligand: stick, cyan:cluster1, magenta:cluster2, yellow:cluster3, light blue: cluster4 and gray:cluster5 and same for (**c**) second conformation, followed by (**d**) third conformation.
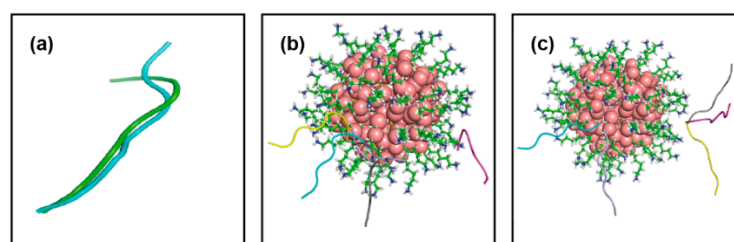

Figure 2. (**a**) Two different conformations for longer peptide, H_3 generated using cluster analysis over simulation. (**b**) Different docking poses obtained for first conformation of H_3 with $Au_{144}(L)_{60}$ and that for (**c**) second conformation, color code is the same as in Figure 1.

2.1.2. MD of Au-MPC in Water

Similarly, RMSD for functionalized ligands for $Au_{144}(L)_{60}$ is being depicted in Figure S1f. The shape and integrity of the nanocluster, conformational fluctuations of the functionalized ligands do not reflect noticeable changes after the simulation with respect to initial configuration. The same clustering protocol (cut-off 0.2 nm) is applied to the Au-MPC, from which a single structure is extracted (Figure 1c) with ~9000 structures over the last 500 ns equilibrated data.

2.2. Binding Poses and Binding Energies of Peptide-Au-MPC Complexes

In Table 1, the docking results and the corresponding driving forces for the H_1 peptide-Au-MPC association complexes are reported for each conformation of the peptide. Unbiased sampling of three different conformations is done in each Brownian dynamics simulation by choosing all of the three conformations randomly during the trajectory [42]. After the solutes' positions and orientations are updated during the BD propagation step, BD moves to alternative coordinate sets using the adjacent conformations in the list and a Metropolis algorithm is used to accept (or refuse) trial moves. We find that in H_1, first conformation is visited for 28.4% times of entire sampling, whereas the second one for 46.5%, and that for the third is 25.1%. However, the final results of docking are obtained after clustering analysis performed over BD trajectories for each of three different conformations separately, to identify different binding pose on the Au-MPC, peptide-nanocluster orientations, free energy of binding, relative population in each cluster and corresponding RMSD. One can identify the most popular and energetically favourable cluster corresponding to each single conformation. Similarly, among three different clusters corresponding to three different conformations, the most suitable one can be chosen primarily based on interaction energy.

Table 1. Peptide (H_1)-nanocluster docking results as obtained from SDA.

Conf Index	Clust Index	RelPop (%) [a]	(U_{Repr}) kT [b]	(U_{EP}) kT [c]	(U_{ds}^e) kT [d]	(U_{ds}^h) kT [e]	Spread [f]
1	**A1**	**70.8**	**−52.815**	**−50.607**	**8.886**	**−11.094**	**1.203**
1	A2	12.0	−51.375	−51.288	9.046	−9.132	1.172
1	A3	7.0	−50.788	−50.638	9.936	−10.085	0.571
1	A4	8.4	−51.005	−51.168	9.391	−9.227	0.343
1	A5	1.8	−51.006	−49.864	9.771	−10.913	0.495
1	**B1**	**63.5**	**−50.890**	**−47.567**	**8.618**	**−11.841**	**0.342**
1	B2	18.9	−50.631	−45.628	7.283	−12.287	0.500
1	B3	11.4	−50.676	−45.877	6.823	−11.622	0.464
1	B4	3.8	−50.268	−47.143	8.347	−11.472	0.254
1	B5	2.4	−50.361	−48.345	8.667	−10.683	0.273
1	**C1**	**37.3**	**−51.075**	**−50.940**	**10.970**	**−11.105**	**0.626**
1	C2	21.7	−51.325	−49.756	9.965	−11.534	0.518
1	C3	33.9	−50.266	−49.160	10.833	−11.940	0.601
1	C4	5.6	−50.346	−50.611	10.391	−10.126	0.387
1	C5	1.5	−50.230	−50.292	10.715	−9.654	0.001

(a) Relative population of this cluster (b) U_{Repr}: total interaction energy of the representative of the given cluster in kT with T = 300 K, (c) U_{EP}: total electrostatic energy of the representative complex, in kT, (d) U_{ds}^e: electrostatic desolvation energy of the representative complex, in kT, (e) U_{ds}^h: hydrophobic desolvation energy of the representative complex, in kT, (f) Spread: RMSD of the structures within the cluster with respect to the representative complex, Å.

In all the resulting complexes, in Figure 1b–d, the binding is dominated by electrostatic interaction, whereas the contribution from non-polar (hydrophobic) desolvation energy (U_{ds}^h) is smaller. However, for peptide conformations 2 and 3, a slight decrease in the electrostatic term is compensated by an increase of the hydrophobic energy term. Among the association complexes, the most populate and energetically more stable complex A1 with peptide conformation 1 (−52.9 kT) (Figure 3a) is selected as a starting point for MD refinement. For this cluster, the contacting residues, namely the peptide residues which lie at distances <3.5 Å from the Au-MPC atoms, are residue 2W, 3D and 4D.

In Table 2, the docking results for H_3 peptide are reported. We observe that in analogy with H_1 also for H_3, electrostatic interactions energy plays a dominant role with respect to electrostatic desolvation and hydrophobic desolvation energy.
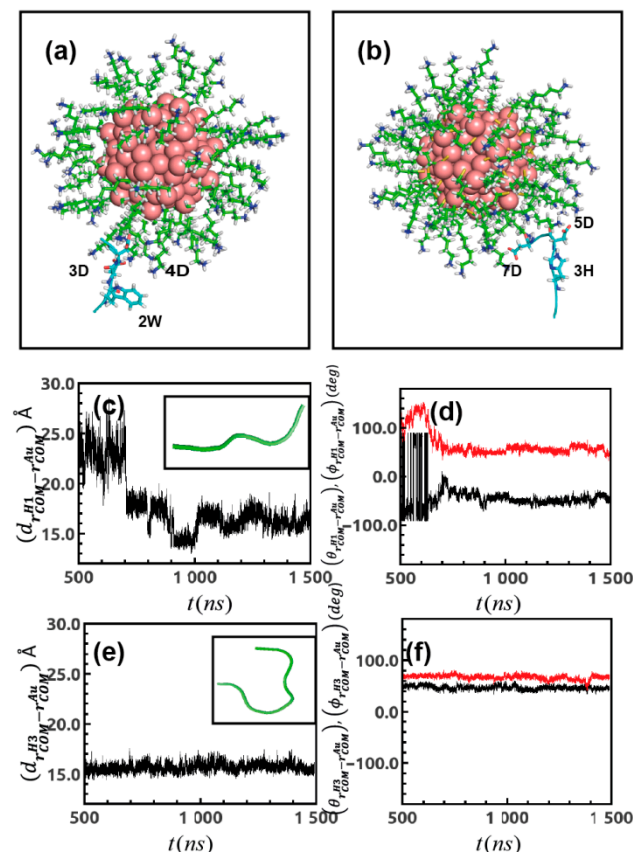
Figure 3. (**a**) Docked structure of H_1 with $Au_{144}(L)_{60}$ and that for (**b**) H_3 with $Au_{144}(L)_{60}$ as obtained from SDA and chosen for MD refinement; contact residues are shown in stick representation (cyan). (**c**) Distance fluctuation between center of mass of H_1 and gold-cluster $\left(d_{r^{H1}_{COM}-r^{Au}_{COM}}(t)\right)$ over simulation time; inset: most popular conformation of the peptide in presence of gold-cluster as generated from equilibrated trajectory. (**d**) Angular representation of $\left(d_{r^{H1}_{COM}-r^{Au}_{COM}}(t)\right)$ as function of *t*. (**e**) $\left(d_{r^{H3}_{COM}-r^{Au}_{COM}}(t)\right)$ vs *t* plot; inset: most crowded conformation of longer peptide H_3 generated after simulation performed in presence of gold-cluster and (**f**) angular component of $\left(d_{r^{H3}_{COM}-r^{Au}_{COM}}(t)\right)$ over simulation time.

Table 2. Peptide (H_3)-nanocluster docking results as obtained from SDA.

Conf Index	Clust Index	RelPop (%) [a]	(U_{Repr}) kT [b]	(U_{EP}) kT [c]	(U^e_{ds}) kT [d]	(U^h_{ds}) kT [e]	Spread [f]
1	**D1**	**78.5**	**−55.104**	**−51.538**	**9.048**	**−12.613**	**1.271**
1	D2	10.7	−53.506	−52.317	10.716	−11.905	0.821
1	D3	3.6	−53.496	−52.045	9.897	−11.347	0.369
1	D4	3.7	−53.642	−50.904	10.819	−13.557	0.292
1	D5	3.5	−53.541	−49.327	9.270	−13.484	0.267
1	**E1**	**44.4**	**−54.087**	**−52.973**	**10.398**	**−11.511**	**2.127**
1	E2	26.2	−54.218	−53.461	9.214	−9.971	1.573
1	E3	15.8	−53.681	−54.362	10.045	−9.364	4.559
1	E4	10.8	−54.442	−51.790	8.913	−11.565	0.578
1	E5	2.8	−53.662	−53.151	9.899	−10.410	1.772

(a) Relative population of this cluster (b) U_{Repr}: total interaction energy of the representative of the given cluster in kT with T = 300 K, (c) U_{EP}: total electrostatic energy of the representative complex, in kT, (d) U^e_{ds}: electrostatic desolvation energy of the representative complex, in kT, (e) U^h_{ds}: hydrophobic desolvation energy of the representative complex, in kT, (f) Spread: RMSD of the structures within the cluster with respect to the representative complex, Å.

The different binding poses are reported in Figure 2b,c and they have comparable

binding energies. However, complex D1 obtained with peptide conformation 1 (Figure 3b) not only has the most favorable binding but it is also the most populated cluster among the others, with a binding free energy -55.1 kT. Thus, this complex is further assessed by MD refinement. The peptide residues involved at the contacting distances are 3H, 5D, 7D. Overall, the docking result indicates that H_3 is able to establish a stronger binding with Au-MPC with respect to H_1.

2.3. MD Simulations of Peptide-Au-MPC Complexes

RMSD for peptides as well as ligands in H_1 bound $Au_{144}(L)_{60}$ system is depicted in Figure S3a,b. RMSD plots for complex (H_3 bound $Au_{144}(L)_{60}$) generated over the simulation are shown in Figure S3c,d.

In the following part, we focus on observables that characterize the relative positions between the peptides and the Au-MPC as well as the changes in their conformations when moving from the free forms in water to the associated forms in the peptide-Au-MPC complex. The relative peptide-cluster distance in each trajectory is tracked using the distance between the COMs of the peptide and the COM of Au-MPC. At first, the coordinates of the COM of the peptide and of the Au core (r_{COM}^{H1} and r_{COM}^{Au} respectively) are computed, then the distance between them $\left(d_{r_{COM}^{H1} - r_{COM}^{Au}}(t) \right)$ is plotted over the last 1.0 µs of the total 1.5 µs simulation time. For H_1 peptide, results are reported in Figure 3c and data indicate that the peptide H_1 approaches the gold cluster in 3 different stages, namely, between 500 and 700 ns the peptide lies quite far (~25 Å) from the Au core, in the time range 700–1000 ns it eventually approaches at closer distances ~17 Å, experiencing a minimum distance of ~15 Å around 1000 ns and in the last stage going from 1000 to 1500 ns it finally gets relaxed within the surface of the monolayer at a distance of ~16 Å. These stages remind of the binding process for peptides on extended surfaces [43,44]. The analysis of these three different dynamic regimes is even more prominent when plotted in polar coordinates (Figure 3d), where instead of $\left(d_{r_{COM}^{H1} - r_{COM}^{Au}}(t) \right)$ we plot the angular coordinate variations $\left(\theta_{r_{COM}^{H1} - r_{COM}^{Au}}(t) \right)$, $\left(\phi_{r_{COM}^{H1} - r_{COM}^{Au}}(t) \right)$. For the H_3 peptide, the variation between center of mass of peptide and gold core $\left(d_{r_{COM}^{H3} - r_{COM}^{Au}}(t) \right)$ is reported in Figure 3e and its polar representations $\left(\theta_{r_{COM}^{H1} - r_{COM}^{Au}}(t) \right)$, $\left(\phi_{r_{COM}^{H1} - r_{COM}^{Au}}(t) \right)$ in Figure 3f as a function of simulation time. Data indicate that unlike the shorter peptide H_1, H_3 experience a fast adsorption dynamics towards the Au-MPC monolayer, relaxing at a distance ~16 Å within the first 500 ns and remains settled at the same distance for the last 1.0 µs of the simulation. The data suggest that a slightly different peptide length may affect the initial phases of the peptide dynamics association towards the Au-MPC.

In order to address the peptide conformational changes induced by the binding to the Au-MPC, clustering algorithm was applied to the last 500 ns of the trajectory. As a result of the interaction with the Au-MPC, H_1 loses its fully stretched conformation observed in the water solvent (see Section 4.3), and it rather prefers to settle in a bit-curved conformation at one end (inset Figure 3c). For peptide H_3, the structure reported in the inset of Figure 3e shows an important change in the conformation of the peptide upon binding to Au-MPC. In fact, it completely loses its stretch conformation to display a more folded one which mimics a "horse shoe" shape (the figure is the result of a clustering analysis including ~10,000 snapshots generated over equilibrated trajectories, Figure S3).

We further generate SASA of the peptide ($SASA_{H1}^{f}$) in the absence as well as in the presence of the Au-MPC ($SASA_{H1}^{nc}$) along the abovementioned time domains of the association dynamics and we generate the corresponding distributions, as represented by H($SASA_{H1}^{f}$) and H($SASA_{H1}^{nc}$) respectively. Figure S4a signifies that H($SASA_{H1}^{f}$) encompasses a broad range of SASA which is similar to nature of H($SASA_{H1}^{nc}$) over 500–700 ns, where the peptide explores the path randomly, finally between 700–1000 ns and 1000–1500 ns H($SASA_{H1}^{nc}$) becomes narrower. Although, quantitatively the SASA values do not differ significantly, they show that the SASA of the peptide gets reduced

upon binding. In analogy with the shorter peptide, SASA of H_3 (Figure S4c) in presence of the nanocluster $(SASA_{H3}^{nc})$ gets reduced with respect to free peptide in water $\left(SASA_{H3}^{f}\right)$.

Similarly, we monitor the difference between the radius of gyration of the peptide in water $\left(R_{gH1}^{f}\right)$ with its distribution $H\left(R_{gH1}^{f}\right)$, and in the presence of the gold cluster $\left(R_{gH1}^{nc}\right)$, $H\left(R_{gH1}^{nc}\right)$. Figure S4b suggests that radius of gyration of the peptide does not get affected by the binding. Also in the case of peptide H_3 the radius of gyration (Figure S4d) $H\left(R_{gH3}^{f}\right)$ and $H\left(R_{gH3}^{nc}\right)$ remain comparable.

We further look into –to-end distance fluctuation of the peptide; we consider distance between N-Terminal tail (i.e., terminal N atom of the first residue in the sequence) and C-Terminal tail (i.e., terminal C atom of the last residue in the sequence) of the peptide and then we monitor the distance variation in two different environments $(d_{end2end\,H1}^{f})$ and $(d_{end2end\,H1}^{nc})$ followed by the corresponding distribution $H(d_{end2end\,H1}^{f})$ and $H(d_{end2end\,H1}^{nc})$. This plots gives us quite interesting results. Mean value of $(d_{end2end\,H1}^{f})$ ~15 Å with broad distribution justifies the stretched conformation of peptide in its free form as reported in Figure 4a, while in presence of the nanocluster during the first 500–700 ns $(d_{end2end\,H1}^{nc})$ undergoes lots of conformational changes with a mean value of $(d_{end2end\,H1}^{nc})$ ~12 Å. The peptide over 700–1000 ns resembles $(d_{end2end\,H1}^{f})$ ~15 Å and then finally achieves bended conformation after stable binding over 1000–15,000 ns with a mean value of $(d_{end2end\,H1}^{nc})$ ~10 Å.
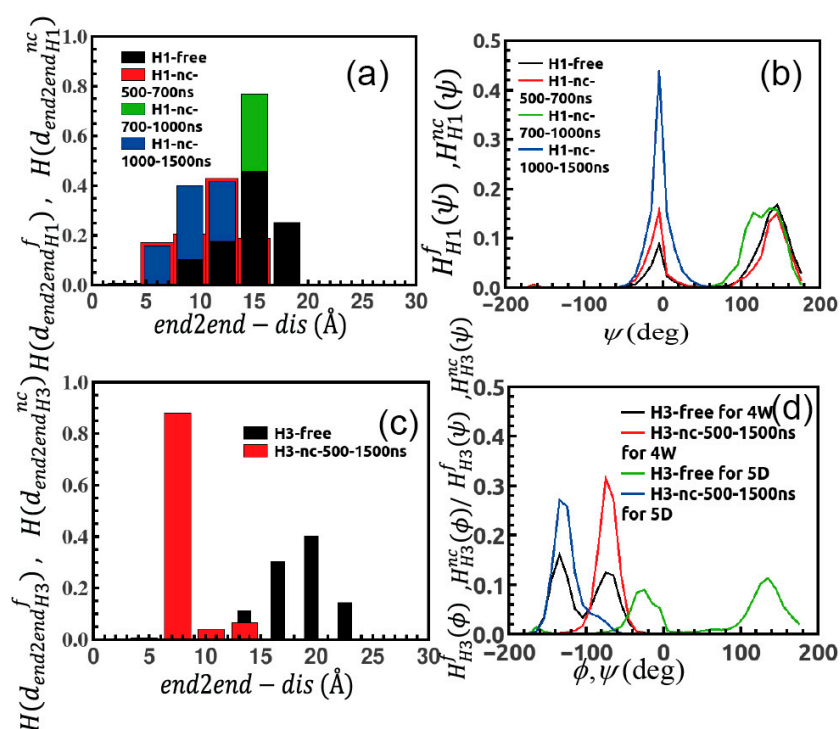

Figure 4. (**a**) Distribution of variation of end-to-end distance of H_1 in free and in presence of gold-cluster; peptide is less stretched in bound form and that for (**b**) distribution of dihedral fluctuation, peptide loses its flexibility in presence of gold cluster. (**c**) Histogram of end-to-end distance for H_3 showing peptide achieves curved conformation in complex state. (**d**) Similarly, dihedrals become less flexible in proximity with nanocluster.

Next, we focus on dihedral fluctuations of the peptide and follow the same protocol to obtain dihedral distribution over simulated trajectories to distinguish between two circumstances. We find that in presence of the nanocluster, peptide loses its flexibility as indicated by some of the representative cases in Figure 4b. The bimodal distribution of dihedral ψ of residue 2W, $H_{H1}^{f}(\psi)$ and $H_{H1}^{nc}(\psi)$ demonstrates that ψ is more flexible in the free state and

up to 1000 ns in presence of the nanocluster, i.e., in the initial period of exploration. Once the peptide forms stable binding on the surface of monolayer, dihedral fluctuates less and $H_{H1}^{nc}(\psi)$ becomes unimodal. We compute MSD (Mean Squared Displacement) of the center of mass for the peptide as a function of simulation time, $\left\langle \left(r_{COM-H1}^{f}\right)^2(t)\right\rangle$ (Figure 5a), and we observe that it has a linear dependence over t which is characteristic of normal diffusion in liquid and the diffusion coefficient (D_{H1}^{f}) is ~0.28×10^{-5} cm^2/s (in good agreement with the HYDROPRO value); however, in proximity of constraint gold cluster the peptide shows deviation from normal diffusion as shown by $\left\langle \left(r_{COM-H1}^{nc}\right)^2(t)\right\rangle$ in Figure 5b–d. As a result, the magnitude of diffusion coefficient (D_{H1}^{nc}) gets reduced eventually over 500–700 ns ~0.08×10^{-5} cm^2/s, 700–1000 ns and then this is more prominent over 700–1000 ns, followed by 1000–1500 ns. This is a signature of diffusion [45,46] and resembles [47] binding dynamics in bio-molecules.
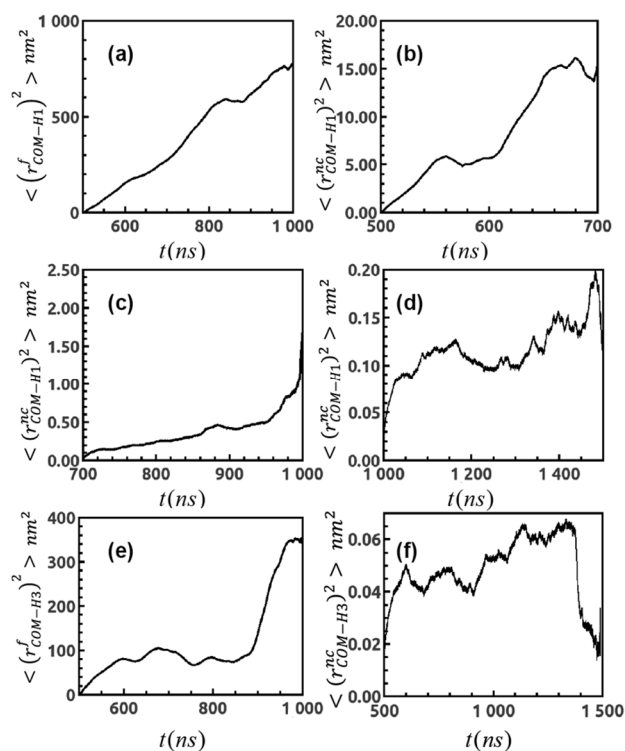

Figure 5. (**a**) MSD plot for center of mass for peptide H$_1$ in free state, indicating normal diffusive behavior and that for in presence of nanocluster in (**b**) for 500–700ns, (**c**) 700–1000 ns, (**d**) 1000–1500 ns demonstrating deviation from linear dependence of MSD over time. (**e**) MSD plot for center of mass for peptide H$_3$ in free and (**f**) in presence of gold cluster signifying signature of binding.

The induced conformational change of H$_3$ peptide is highlighted in Figure 4c. In its free state, the peptide prefers to remain in a fully stretched conformation with a mean value of ($d_{end2end\,H3}^{f}$) ~17 Å, while in its bound form it assumes a more curved conformation along with average value ($d_{end2end\,H3}^{nc}$) ~7 Å. Similarly, the peptide dihedrals lose their flexibility in the bound state (Figure 4d); bimodal dihedral distribution of residue 4 W ($H_{H3}^{f}(\psi)$) and that of residue 5D ($H_{H3}^{f}(\phi)$) transfer into unimodal form ($H_{H3}^{nc}(\psi)$), ($H_{H3}^{nc}(\phi)$). Besides, MSD plots $\left\langle \left(r_{COM-H3}^{f}\right)^2(t)\right\rangle$ and $\left\langle \left(r_{COM-H3}^{nc}\right)^2(t)\right\rangle$ in Figure 5e,f demonstrate that peptide follows normal diffusive motion with diffusion coefficient (D_{H3}^{f}) is ~0.19×10^{-5} cm^2/s (again in line with HYDROPRO results), while in the vicinity of Au-MPCs it carries nonlinear dependence of MSD over time t.

Ultimately, we identify the ligands of the Au-MPC forming direct contacts with the peptides. First, we compute distance between all atoms of the peptide and the terminal

amine N atom of the ligands and then sort the ones that come ≤ 3 Å over simulated trajectories. Then, we generate probability of finding the ligands as per contact as $P\left(close_{H1}^{lig}\right)$ (Figure 6a) and then also point out the ligands that come close to the peptide simultaneously over simulated data (Figure 6b and Figure S5a,b). We observe that there are groups of ligands that are initiating the binding over the 500–700 ns time domain forming a transient binding pocket for the peptide, followed by another group of ligands contacting the peptide over the 700–1000 ns stage and finally a group of ligands which belong to a stable binding patch over the last stage. This means that peptide explores a large share of the surface of the monolayer before finding suitable binding location. We also identify that the peptide is forming contact primarily via the carbonyl O atom of 1H, the side chain carboxyl oxygens of 4D and 5D and the terminal carboxyl oxygen of the 6D residues. However, there are some ligands (id: 12, 26, 33, 34, 35, 40) which form strong binding over the entire last 500 ns of the trajectory, possible by forming contacts with multiple residues at the same time (representative cases are in Figure S6a,b) while some of the ligands (3, 21, 56) (Figure S6c,d) form transient weaker binding patch by showing back and forth motion towards peptide spanning a broad distance between 3 to 20 Å over simulation. Next, we probe inter-ligand fluctuations of the ligands belonging to the binding patch for the peptide. We address distance fluctuation between terminal N atoms of those ligands over simulation (Figure S7a,b); they come in proximity with each other with a mean value of distance of ~5 Å. The final binding pose is depicted in Figure 5c. This event resembles studies [48] on formation of transient protein like binding pocket; mimicking protein–ligand recognition mechanism formed by functionalized monolayer protected gold nanocluster or that for designing nanoreceptors with targeted affinity [49].
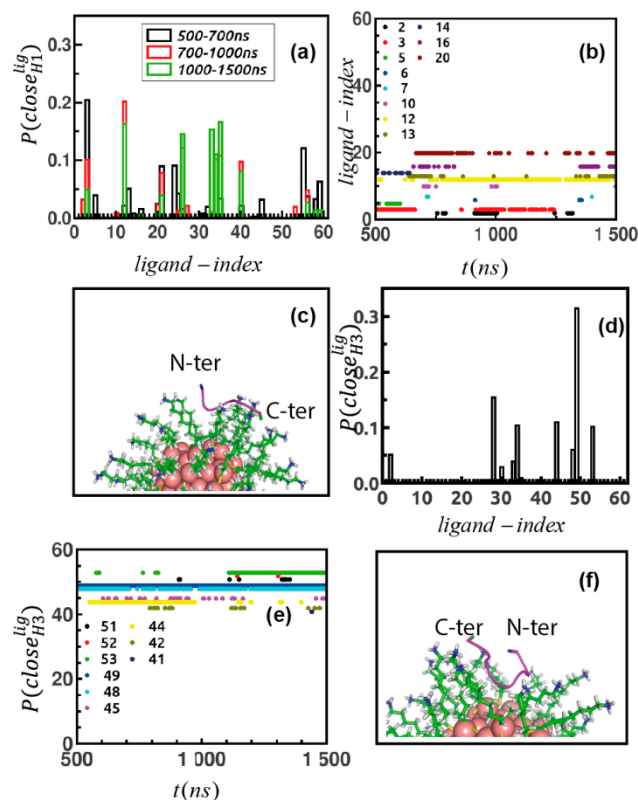

Figure 6. (**a**) Statistical plot of ligands showing strong contribution in binding with peptide H_1. (**b**) Ligands that make contact with peptide H_1 simultaneously over simulation time. (**c**) Final binding orientation of H_1 bound $Au_{144}(L)_{60}$; ligand in cyan, stick mode, peptide in magenta, binding residue terminal ASP are in red and N Histidine is in blue, CPK representation. (**d**) Contributing ligands in binding with H_3. (**e**) Ligands making simultaneous contact with H_3 over simulation time and (**f**) final structure of H_3 with $Au_{144}(L)_{60}$, color code is same as Figure 6c.

The same plots are produced for H_3 to disclose the ligands forming direct contact with H_3, namely $P\left(close_{H3}^{lig}\right)$ in Figure 6d and to distinguish the ones forming contact points simultaneously (Figure 6e and Figure S5c,d) over the simulation. Here, also 2H, 5D, 6D and 7D residue networks participate in binding across monolayer, followed by a group of ligands manifesting strong interaction (Figure S6e,f) with multiple and consistent contact patches. Some exhibit weaker connectivity (Figure S6g,h). The final binding pose is depicted in Figure 6f. The connectivity between ligands belonging to the binding networks is shown by distance fluctuation over simulation in Figure S7c,d.

In our next analysis, we probe pair correlation function between the S atom of the thiol group and the central Aspartic acid residue of both the peptide sequences ($g_{S-ASP}^{H1-nc}(r)$, $g_{S-ASP}^{H3-nc}(r)$) over simulation data. This gives us a better idea regarding spatial arrangement of peptides around monolayer. We observe that during 700–1000 ns, H_1 penetrates into a channel formed by adjacent monolayers; however, the peptide does not remain inside the channel for too long; in its stable binding mode it settles over the surface of layer, which is followed by H_3 in its bound form (Figure S8a,b, snapshots in Figure S8c,d).

The secondary structures content for the free peptide in solution and for the peptide complexed with the nanocluster has been computed using the DSSP in-built algorithm of (VMD) [50]. Figure S9a,d indicates that the overall effect of the Au-MPC on both peptides is to increase the β-turn propensity with respect to the random coil. This effect is more prominent in the case of H_3. We then compute the stability [51] of the peptides in terms of the number of contacts in the final conformations and in different environments using Go$^-$ contact map analysis [52,53]. The Go$^-$ coarse grained model is based on a lower resolution description of the peptide in which beads are located at C_α position. For the present application, a fully atomistic force field represents a very good balance between accuracy and computational feasibility. For longer peptides, simplified schemes such as coarse grained descriptions (e.g., the recent Go-MARTINI FF for peptide) should also be considered, although such FFs should be extended to the nanocluster as well. More specifically, the analysis is based on contact generated from native structure and interacting through LJ potential and it represents an established method to understand conformational transition in proteins. When the method is applied to our peptides, we find the presence of native contacts, only between residues 1H and 6D of H_3 peptide in the presence of nanocluster, based on the standard distance threshold and sequence distance cut-off. No contact map is observed in the corresponding free state of the same peptide. This implies the presence of significant changes in the peptide conformation occurring only in the longer peptide sequence and its bound form.

3. Discussion

We find that if the peptide has more catalytically active residues in its sequence, it forms stronger, stable and faster binding network across the monolayer. Besides, it also undergoes drastic changes in conformation showing two different but specific orientations for the two peptides in a regime of non-rigid binding to the Au-MPC. H_3 prefers to remain in horse-shoe-shaped conformation unlike the stretched one and the loss of flexibility is also more prominent here.

Thus, we realize that the surface of the monolayer is the suitable location for formation of stable binding, if the peptide penetrates into cavity formed by functionalized ligands then Histidine will not be favorable for catalysis; the larger the sequence, the lesser the probability to get buried inside, as a result faster and stronger is the binding. The reduction in number of intra-molecular H-bond network for imidazole N atoms of Histidine in presence of monolayer is more pronounced (Table S1) for H_3 than H_1, which can be a potential cause for making imidazole more available [54] for trans-esterification.

We observe that while both peptides prefer to remain in stretched conformation in absence of the cluster, the Au-MPC induces reduced flexibility, followed by a curved conformation, and a decrease in the number of intra-molecular hydrogen bonds especially for Histidine. All these changes are in line with an increase in the catalytic power of the bound

peptide compared to the unbound one, in agreement with the experimental findings [41]. These changes become more prominent for the longer peptide with more Histidine; for the shorter peptide, formation of transient binding moieties by the functionalized ligands almost over the entire monolayer surface are more significant. On the other hand, for the longer peptide the binding is stronger and faster. Thus, we highlight a potential correlation between peptide length and increased rate constant of trans-esterification based on microscopic information using MD simulation that goes beyond the simple availability of a larger number of catalytic residues.

4. Materials and Methods

MD simulations at all-atom to coarse-grained scales are assessed tools for the study of non-static binding partners such as that involving a peptide (or protein) and a NP [55–58]. The difficulty in identifying the preferred orientation of biomolecules toward a given NP using MD simulations is due to the existence of many putative binding poses on the NP, nearly degenerate in energy, associated to the quite uniformity of the NP. We wish to remark that one of the main aims of the present study was that of disclosing the dynamics of the peptide association on the surface of Au-MPC. Hence, by performing metadynamics and/or other enhanced sampling simulations, we would have forced the dynamics of the system along a given collective variable, thus we would have lost a faithful temporal evolution of the binding association process. We proceed with 1 μs long MD simulation of peptides and nanocluster separately, followed by an unbiased sampling of different peptide conformations on top of Au-MPC. We sample the initial conditions by means of flexible Brownian Dynamics (BD) simulations, to remove biases that could lead to local minima in the binding process if simulated directly by atomistic MD. Additionally, a conformational sampling of the flexible peptide in water and during the association dynamics is taken into account by classical MD. This allows using MD simulations to predict properties of the peptide-Au-MPC complexes such as amino acid-specific interactions with NP ligands and supramolecular structure that ultimately drive the formation and the catalytic activity of peptide-NP conjugates.

Being aware that the results are affected by the quality of FF parameters used for the Au-MPC, we have developed ad hoc parameters for the system based on ab initio calculations and following the same strategy used to develop GolP [59] but taking explicitly into account the chemical nature of the ligand groups. Ligands are parameterized with OPLS/AA force field [60] and sulphur and gold atoms are parametrized as described before [61]. Gold polarization is neglected because the binding between the peptide and the Au-MPC is occurring through the ligand atoms of the monolayer and not directly through gold core atoms. The highly charged self-assembled monolayer makes the electrostatic interactions dominant, thus, polarization of gold atoms does not play a significant role in this kind of monolayer protected gold cluster.

The GolP FF has been originally developed for large bare gold NP (modelled ad flat surfaces) [59] and firstly extended to citrated capped gold NP [62]. The parameterization has been proved to be able to reproduce NMR chemical shifts of large proteins, e.g., Ubiquitin and β2-microglobulin, on citrate-capped gold NP [62–64]. The FF has been further tested and validated on the absorption of β2-microglobulin on differently functionalized small gold NPs [62,63].

In this work, a multi-step computational pipeline is used that includes: (i) 1 μs MD simulations of the peptide in water (without the Au-MPC) providing an initial extensive conformational sampling, crucial for the description of the relevant phases of the peptide adsorption process, (ii) flexible Brownian Dynamics (BD) including multiple flexible conformations of the peptide and a rigid body representation of the Au-MPC in implicit solvents, (iii) 1.5 μs MD refinement simulations of the most relevant peptide-Au-MPC complex resulting from the clustering analysis of the BD trajectories. The protocol is based on different software packages implemented in a compatible way at the different scales,

i.e., the SDA7.2.2 software [42] and the GROMACS package [65] for MD simulations using the newly developed Au-MPC FF within extended GolP [59].

4.1. Set-Up of the H_1 and H_3 Peptide Systems

Two peptide sequences, namely, HWDDD (H_1) and HHHWDDD (H_3), are simulated in aqueous solvent. The initial structure of the peptides is obtained using Swiss-PDB Viewer which is the graphical counter part of the Swiss Model repository [66]. The 3D model of the target sequence is obtained after aligning it over a known structure of sequence similarity, followed by energy minimization to obtain the secondary structural assignment. The initial structure of the peptide H_1 is shown in Figure S1a. OPLS/AA force field parameters [60] are used for the peptide in its neutral protonation state, SPC/E water model [67] is used within GROMACS-5.0.4 version [65,68] in a cubic box with a 4 nm side, using periodic boundary condition [45,46]. The system contains 5186 atoms; 3 Na^+ ions are added to guarantee the neutrality of the system. Initially, the entire system is minimized for 50,000 steps using steepest descent algorithm [69], followed by 100 picosecond (ps) isothermal isochoric (NVT) and 100 ps isothermal isobaric (NPT) equilibration. The Bussi-Donadio-Parrinello [70] thermostat is used to maintain temperature at 300 K and for pressure coupling at 1 bar Parrinello–Rahman [71] barostat is used. Simulation time step 2 femtosecond (fs) is chosen and Newton's equation of motion is solved using leap-frog algorithm, short range cutoff for van der Waals and electrostatic interaction is ~1.0 nm, LINCS algorithm is used to constrain bond length and Maxwell Boltzmann distribution is considered to assign velocity [45,46]. Particle Mesh Ewald method [72] is used to take into account long ranged interaction, trajectory is saved every 10 ps. Finally, 1 μs simulation at neutral pH (we have used the standard protonation state of Histidine according to the experimental [41] pH = 7, as the pKa value of Histidine side chain is <7, we consider a neutral protonation state for the residue), room temperature and ~10 mM ionic strength is performed and the analyses are done over last 500 ns data. The same protocol is followed to build the structure of H_3, namely HHHWDDD peptide (initial structure in Figure S1b) and to perform 1 μs simulation trajectory.

4.2. Set-Up of the Nanocluster Model $Au_{144}(L)_{60}$ ($L = S(CH_2)_8NH_2^+$)

A 3D model for the functionalized gold nanocluster compatible with GROMACS engine is initially built with 'NanoModeler' [73] from which an initial geometry is obtained. The geometry is built from the webserver first assigning the correct morphology to core gold atoms Au144 and its staple-like motif (see Figure S2), which are connecting the S ligand atoms to gold surface (AUS) and gold interface (AUL) atoms [74]. Finally, the ligands are processed to form a homogeneously assembled monolayer. However, the resulting topology for the entire complex is generated using AMBER force field [74], where only non-bonded [75] interactions are incorporated for gold atoms without assigning charge or any bonding parameters. Thus, OPLS/AA FF parameters are developed for the Au-MPC compatible with the previously developed GolP FF [61]. For the entire Au-MPC (Figure S1c), OPLS/AA topology is generated using TPPmktop server [76] and LJ parameters for Au atoms are taken from GolP. Finally, RESP [77] (Restrained electrostatic potential) charges are explicitly derived for all the atoms belonging to the smallest Au-MPC surface repeating unit, namely AUS-RS−AUL−SR-AUS. Where SR is the alkanethiol functional groups connected to the core through a sulfur atom forming the "staples" (see Figure S2), S is the sulfur atom forming a covalent bond with one gold atom at the interface (AUL = gold ligand) and a gold atom at the surface (AUS = gold surface). The charges are derived using R.E.D. server [78]. FF parameters are derived according to a strategy already used for different gold NPs which has been already extensively tested [61,79].

A cubic simulation box of dimension 6 nm is built and neutralized by adding 60 CL. Gold core atoms are kept frozen during equilibration and production run to maintain integrity of the structure, while the interfacial surface atoms are relaxed. Nose-hoover Thermostat [80] is used to achieve NVT equilibration, namely, 1 ns NVT equilibration

is performed by keeping the entire nanocluster fixed (to capture electrostatic screening generated by ions [81]), to allow the ions to relax around the NP monolayers in water-box and then the self-assembled layer is freely relaxed for another 1 ns including ions and water molecules for temperature coupling. One μs production run is performed and post-processing analyses are performed on the trajectories collected in the last 500 ns.

4.3. Set-Up of the Flexible Docking Simulations

The flexible docking used in this work and implemented on SDA7.2.2 software [42] allows more than one rigid structure of the peptide to be included, thus incorporating peptide conformational flexibility into the BD simulations. The initial structures of peptides H_1 and H_3 to be included in the flexible docking are extracted from the 1 μs MD trajectories after clustering analysis (details in Section 2.1). Thus, three different conformations of H_1, two for H_3 and one for nanocluster (rigid conformation) are chosen to start the Brownian Simulation including flexible docking within SDA7.2.2. code [42,82].

Total interaction energy (U_{Repr}) between two solutes is computed as the summation of (a) long-range electrostatic interactions (U_{EP}) between the pair, (b) component associated with short range electrostatic desolvation (U_{ds}^{e}), (c) non-polar desolvation resembling hydrophobic collapse (U_{ds}^{h}) (More details in SI).

A grid dimension of $161 \times 161 \times 161$ A^3 is used to build the electrostatic potential grid with a grid spacing of 1.0 Å using APBS program [83], including 10 mM ionic strength, the dielectric constant of the water solvent (78.0 at room temperature ~300 K) and of protein interior (2.0). For each system, 5000 runs are performed to identify peptide preferred binding orientation on the Au-MPC and the corresponding trajectories are collected, each with 500 ns simulation time. Typically, this type of simulation is performed within a box of spherical symmetry, at first the center of one solute is placed at 100 Å distance from the center of the other solute. Simulation time step is chosen 1 ps as long as the center-to-center distance between those two solutes remains <50 Å. For the nanocluster terminal N atoms and for the peptide O atoms of side chain of residue D, they are considered to calculate effective charges. The translational diffusion coefficient for the peptide is set to 0.27×10^{-5} cm^2/s and for the gold nanocluster is set to 0.11×10^{-5} cm^2/s according to HY-DROPRO [84] software, whereas rotational diffusional coefficients are 30.7×10^{-5} rad^2/ps and 2.1×10^{-5} rad^2/ps for the peptide and the cluster, respectively. The 1000 lowest energy configurations are saved, two different docking positions of the solute are considered based on a threshold root mean square deviation (RMSD) 1 Å between these two configurations. For H_3, the translational diffusion coefficient is set to 0.25×10^{-5} cm^2/s and the rotational diffusional coefficient 22.8×10^{-5} rad^2/ps.

4.4. Set-Up of the MD Refinement of Supramolecular Complexes

The most populated and energetically favourable peptide-Au-MPC association complexes resulting from the flexible docking are refined by 1.5 μs MD. At first, the peptide center of mass is translated by 5 Å with respect to the center of mass of the Au-MPC, without altering the binding orientation of the docking pose. Following our previous studies [61], the procedure is employed to avoid kinetic trapping of the peptide on the surface of Au-MPC, which can lead to the lack of a proper relaxation of the peptide over the surface. For peptide H_1, a cubic simulation box is used with dimension set to 7 nm, and 34,382 atoms including 57 Cl$^-$ ions are added. All the other technical details of the simulation are the same as those used for simulations of Au$_{144}$(L)$_{60}$ cluster in aqueous solvent. A gradual NVT equilibration is performed, at first only ions and water molecules are relaxed, then also interfacial ligands atoms are relaxed and finally the entire system is freely relaxed in explicit solvent (keeping core gold atoms frozen) for 1 ns. Finally, 1.5 μs simulation of production run are performed. The same MD refinement protocol is applied to the H_3-Au-MPC complexes resulting from docking. A cubic box of dimension 7 nm was used with a total number of atoms equal to 37,513. Next, 1.5 μs simulation is performed and followed by the analysis.

4.5. Analysis of MD Trajectories

We used Visual Molecular Dynamics (VMD) [50] and PyMoL [85] software to visualize trajectories over simulation time. RMSD is computed to ensure equilibration of the simulation. SASA, radius of gyration, pair correlation function, mean square displacement (MSD) and cluster analysis are some of the parameters that are being analysed (details in SI). All other calculations to extract information about microscopic properties of the systems are computed using in house codes.

5. Conclusions

In the present study, we have shown how a computational protocol that involves development of new atomistic force field parameters, flexible docking with Brownian Dynamics and µs-long MD simulations can be useful to gain the microscopic picture at the basis of experimental results for complicated bio-nanosystems such as nanozymes. In particular, in our study, we emphasized the collective effects of peptide sequence length, peptide conformation, dihedral flexibility, underlying structure dynamics of binding mode between peptide-Au-MPCs, and the potential role of H-bond network in modulating catalytic activity of this supramolecular assembly. The computational methodology described here can be useful for other problems within this class, such as to tune not only catalytically active peptide-nano conjugate but also to design proper nanoreceptor with target affinity in domain of nanomedicine and industrial applications in future.

References

1. Pasquato, L.; Pengo, P.; Scrimin, P. Nanozymes: Functional Nanoparticle-based Catalysts. *Supramol. Chem.* **2005**, *17*, 163–171. [CrossRef]
2. Manea, F.; Houillon, F.B.; Pasquato, L.; Scrimin, P. Nanozymes: Gold-nanoparticle-based transphosphorylation catalysts. *Angew. Chem.* **2004**, *43*, 6165–6169. [CrossRef]
3. Wang, Q.; Wei, H.; Zhang, Z.; Wang, E.; Dong, S. Nanozyme: An emerging alternative to natural enzyme for biosensing and immunoassay. *Trends Anal. Chem.* **2018**, *105*, 218–224. [CrossRef]
4. Huang, Y.; Ren, J.; Qu, X. Nanozymes: Classification, Catalytic Mechanisms, Activity Regulation, and Applications. *Chem. Rev.* **2019**, *119*, 4357–4412. [CrossRef]
5. Jiang, D.; Ni, D.; Rosenkrans, Z.T.; Huang, P.; Yan, X.; Cai, W. Nanozyme: New horizons for responsive biomedical applications. *Chem. Soc. Rev.* **2019**, *48*, 3683–3704. [CrossRef]

6.   Wang, P.; Wang, T.; Hong, J.; Yan, X.; Liang, M. Nanozymes: A New Disease Imaging Strategy. *Front. Bioeng. Biotechnol.* **2020**, *8*, 15. [CrossRef]

7.   Stasyuk, N.; Smutok, O.; Demkiv, O.; Prokopiv, T.; Gayda, G.; Nisnevitch, M.; Gonchar, M. Synthesis, Catalytic Proper-ties and Application in Biosensorics of Nanozymes and Electronanocatalysts: A Review. *Sensors* **2020**, *20*, 4509. [CrossRef]

8.   Gabrielli, L.; Prins, L.J.; Rastrelli, F.; Mancin, F.; Scrimin, P. Hydrolytic Nanozymes. *Eur. J. Org. Chem.* **2020**, *32*, 5044–5055. [CrossRef]

9.   Das, R.; Landis, R.F.; Tonga, G.Y.; Cao-Milán, R.; Luther, D.C.; Rotello, V.M. Control of Intra-versus Extracellular Bioorthogonal Catalysis Using Surface-Engineered Nanozymes. *ACS Nano* **2019**, *13*, 229–235. [CrossRef]

10. Cao-Milán, R.; He, L.D.; Shorkey, S.; Tonga, G.Y.; Wang, L.-S.; Zhang, X.; Uddin, I.; Das, R.; Sulak, M.; Rotello, V.M. Modulating the catalytic activity of enzyme-like nanoparticles through their surface functionalization. *Mol. Syst. Des. Eng.* **2017**, *2*, 624–628. [CrossRef]

11. Cao-Milán, R.; Gopalakrishnan, S.; He, L.D.; Huang, R.; Wang, L.-S.; Castellanos, L.; Luther, D.C.; Landis, R.F.; Makabenta, J.M.V.; Li, C.-H.; et al. Thermally Gated Bio-orthogonal Nanozymes with Supramolecularly Confined Porphyrin Catalysts for Antimicrobial Uses. *Chem* **2020**, *6*, 1113–1124. [CrossRef]

12. Lou-Franco, J.; Das, B.; Elliott, C.; Cao, C. Gold Nanozymes: From Concept to Biomedical Applications. *Nano-Micro Lett.* **2021**, *13*, 1–36. [CrossRef]

13. Pieters, G.; Prins, L.J. Catalytic self-assembled monolayers on gold nanoparticles. *New J. Chem.* **2012**, *36*, 1931–1939. [CrossRef]

14. Taguchi, T.; Isozaki, K.; Miki, K. Enhanced Catalytic Activity of Self-Assembled-Monolayer-Capped Gold Nanoparticles. *Adv. Mater.* **2012**, *24*, 6462–6467. [CrossRef]

15. Higaki, T.; Li, Y.; Zhao, S.; Li, Q.; Li, S.; Du, X.S.; Yang, S.; Chai, J.; Jin, R. Atomically Tailored Gold Nanoclusters for Catalytic Application. *Angew. Chem.* **2019**, *58*, 8291–8302. [CrossRef]

16. Duncan, K.L.; Ulijn, R.V. Short Peptides in Minimalistic Biocatalyst Design. *Biocatalysis* **2015**, *1*, 67–81. [CrossRef]

17. Pengo, P.; Baltzer, L.; Pasquato, L.; Scrimin, P. Substrate modulation of the activity of an artificial nanoesterase made of peptide-functionalized gold nanoparticles. *Angew. Chem.* **2007**, *46*, 400–404. [CrossRef] [PubMed]

18. Levy, R. Peptide-capped gold nanoparticles: Towards artificial proteins. *ChemBioChem Eur. J. Chem. Biol.* **2006**, *7*, 1141–1145. [CrossRef] [PubMed]

19. Mikolajczak, D.J.; Koksch, B. Peptide-Gold Nanoparticle Conjugates as Sequential Cascade Catalysts. *ChemCatChem* **2018**, *10*, 4324–4328. [CrossRef]

20. Duchesne, L.; Wells, G.; Fernig, D.G.; Harris, S.A.; Lévy, R.; Wells, G. Supramolecular Domains in Mixed Peptide Self-Assembled Monolayers on Gold Nanoparticles. *ChemBioChem* **2008**, *9*, 2127–2134. [CrossRef] [PubMed]

21. Yuan, Q.; Wang, Y.; Zhao, L.; Liu, R.; Gao, F.-P.; Gao, L.; Gao, X. Peptide protected gold clusters: Chemical synthesis and biomedical applications. *Nanoscale* **2016**, *8*, 12095–12104. [CrossRef] [PubMed]

22. Kyrychenko, A. NANOGOLD decorated by pHLIP peptide: Comparative force field study. *Phys. Chem. Chem. Phys.* **2015**, *17*, 12648–12660. [CrossRef] [PubMed]

23. Colangelo, E.; Chen, Q.; Davidson, A.M.; Paramelle, D.; Sullivan, M.B.; Volk, M.; Levy, R. Computational and Experi-mental Investigation of the Structure of Peptide Monolayers on Gold Nanoparticles. *Langmuir ACS J. Surf. Colloids* **2017**, *33*, 438–449. [CrossRef] [PubMed]

24. Samieegohar, M.; Sha, F.; Clayborne, A.Z.; Wei, T. ReaxFF MD Simulations of Peptide-Grafted Gold Nanoparticles. *Langmuir* **2019**, *35*, 5029–5036. [CrossRef]

25. Monti, S.; Barcaro, G.; Sementa, L.; Carravetta, V.; Ågren, H. Dynamics and self-assembly of bio-functionalized gold nanoparticles in solution: Reactive molecular dynamics simulations. *Nano Res.* **2018**, *11*, 1757–1767. [CrossRef]

26. Chew, A.K.; Dallin, B.C.; Van Lehn, R.C. The Interplay of Ligand Properties and Core Size Dictates the Hydrophobi-city of Monolayer-Protected Gold Nanoparticles. *ACS Nano* **2021**, *15*, 4534–4545. [CrossRef]

27. Chew, A.K.; Van Lehn, R.C. Effect of Core Morphology on the Structural Asymmetry of Alkanethiol Monolayer Pro-tected Gold Nanoparticles. *J. Phys. Chem. C* **2018**, *122*, 26288–26297. [CrossRef]

28. Van Lehn, R.C.; Alexander-Katz, A. Structure of Mixed-Monolayer-Protected Nanoparticles in Aqueous Salt Solution from Atomistic Molecular Dynamics Simulations. *J. Phys. Chem. C* **2013**, *117*, 20104–20115. [CrossRef]

29. Kyrychenko, A.; Korsun, O.M.; Gubin, I.I.; Kovalenko, S.M.; Kalugin, O.N. Atomistic Simulations of Coating of Silver Nanoparti-cles with Poly(vinylpyrrolidone) Oligomers: Effect of Oligomer Chain Length. *J. Phys. Chem. C* **2015**, *119*, 7888–7899. [CrossRef]

30. Kyrychenko, A.; Pasko, D.A.; Kalugin, O.N. Poly(vinyl alcohol) as a water protecting agent for silver nanoparticles: The role of polymer size and structure. *Phys. Chem. Chem. Phys.* **2017**, *19*, 8742–8756. [CrossRef] [PubMed]

31. Kyrychenko, A.; Blazhynska, M.M.; Kalugin, O.N. Protonation-dependent adsorption of polyarginine onto silver na-noparticles. *J. Appl. Phys.* **2020**, *127*, 075502. [CrossRef]

32. Tavanti, F.; Pedone, A.; Menziani, M.C.; Alexander-Katz, A. Computational Insights into the Binding of Monolayer-Capped Gold Nanoparticles onto Amyloid-beta Fibrils. *ACS Chem. Neurosci.* **2020**, *11*, 3153–3160. [CrossRef] [PubMed]

33. Sen, S.; Vukovic, L.; Kral, P. Computational screening of nanoparticles coupling to Abeta40 peptides and fibrils. *Sci. Rep.* **2019**, *9*, 17804. [CrossRef]

34. Tavanti, F.; Pedone, A.; Menziani, M.C. Disclosing the Interaction of Gold Nanoparticles with Abeta(1-40) Monomers through Replica Exchange Molecular Dynamics Simulations. *Int. J. Mol. Sci.* **2020**, *22*, 26. [CrossRef] [PubMed]

35. Tavanti, F.; Pedone, A.; Menziani, M.C. Multiscale Molecular Dynamics Simulation of Multiple Protein Adsorption on Gold Nanoparticles. *Int. J. Mol. Sci.* **2019**, *20*, 3539. [CrossRef]

36. Power, D.; Rouse, I.; Poggio, S.; Brandt, E.; Lopez, H.; Lyubartsev, A.; Lobaskin, V. A multiscale model of protein ad-sorption on a nanoparticle surface. *Model. Simul. Mater. Sci. Eng.* **2019**, *27*, 084003. [CrossRef]

37. Tavanti, F.; Pedone, A.; Menziani, M.C. A closer look into the ubiquitin corona on gold nanoparticles by computation-al studies. *New J. Chem.* **2015**, *39*, 2474–2482. [CrossRef]

38. Tavanti, F.; Pedone, A.; Menziani, M.C. Competitive Binding of Proteins to Gold Nanoparticles Disclosed by Molecular Dynamics Simulations. *J. Phys. Chem. C* **2015**, *119*, 22172–22180. [CrossRef]

39. Lopez, H.; Lobaskin, V. Coarse-grained model of adsorption of blood plasma proteins onto nanoparticles. *J. Chem. Phys.* **2015**, *143*, 243138. [CrossRef]

40. Mikolajczak, D.J.; Heier, J.L.; Schade, B.; Koksch, B. Catalytic Activity of Peptide–Nanoparticle Conjugates Regulated by a Conformational Change. *Biomacromolecules* **2017**, *18*, 3557–3562. [CrossRef] [PubMed]

41. Zaramella, D.; Scrimin, P.; Prins, L.J. Self-Assembly of a Catalytic Multivalent Peptide–Nanoparticle Complex. *J. Am. Chem. Soc.* **2012**, *134*, 8396–8399. [CrossRef] [PubMed]

42. Martinez, M.; Bruce, N.J.; Romanowska, J.; Kokh, D.B.; Ozboyaci, M.; Yu, X.; Ozturk, M.A.; Richter, S.; Wade, R.C. SDA 7: A modular and parallel implementation of the simulation of diffusional association software. *J. Comput. Chem.* **2015**, *36*, 1631–1645. [CrossRef] [PubMed]

43. Bellucci, L.; Corni, S. Interaction with a Gold Surface Reshapes the Free Energy Landscape of Alanine Dipeptide. *J. Phys. Chem. C* **2014**, *118*, 11357–11364. [CrossRef]

44. Penna, M.J.; Mijajlovic, M.; Biggs, M.J. Molecular-Level Understanding of Protein Adsorption at the Interface between Water and a Strongly Interacting Uncharged Solid Surface. *J. Am. Chem. Soc.* **2014**, *136*, 5323–5331. [CrossRef]

45. Frenkel, D.; Smit, B. *Understanding Molecular Simulation from Alogorithms to Applications*; Academic Press: Cambridge, MA, USA, 2002.

46. Allen, M.P.; Tildesley, D.J. *Computer Simulation of Liquids*, 2nd ed.; Oxford Science Publications: Oxford, UK, 1989.

47. Banks, D.S.; Fradin, C. Anomalous Diffusion of Proteins Due to Molecular Crowding. *Biophys. J.* **2005**, *89*, 2960–2971. [CrossRef] [PubMed]

48. Riccardi, L.; Gabrielli, L.; Sun, X.; De Biasi, F.; Rastrelli, F.; Mancin, F.; De Vivo, M. Nanoparticle-Based Receptors Mimic Protein-Ligand Recognition. *Chem* **2017**, *3*, 92–109. [CrossRef]

49. Sun, X.; Riccardi, L.; De Biasi, F.; Rastrelli, F.; De Vivo, M.; Mancin, F. Molecular-Dynamics-Simulation-Directed Rational Design of Nanoreceptors with Targeted Affinity. *Angew. Chem.* **2019**, *58*, 7702–7707. [CrossRef] [PubMed]

50. Humphrey, W.; Dalke, A.; Schulten, K. VMD: Visual molecular dynamics. *J. Mol. Graph.* **1996**, *14*, 33–38. [CrossRef]

51. Poma, A.B.; Guzman, H.V.; Li, M.S.; Theodorakis, P.E. Mechanical and thermodynamic properties of Abeta42, Abeta40, and alpha-synuclein fibrils: A coarse-grained method to complement experimental studies. *Beilstein J. Nanotechnol.* **2019**, *10*, 500–513. [CrossRef]

52. Poma, A.B.; Cieplak, M.; Theodorakis, P.E. Combining the MARTINI and Structure-Based Coarse-Grained Approaches for the Molecular Dynamics Studies of Conformational Transitions in Proteins. *J. Chem. Theory Comput.* **2017**, *13*, 1366–1374. [CrossRef]

53. Mahmood, M.I.; Poma, A.B.; Okazaki, K.I. Optimizing Go-MARTINI Coarse-Grained Model for F-BAR Protein on Lipid Membrane. *Front. Mol. Biosci.* **2021**, *8*, 619381. [CrossRef]

54. Byler, K.G.; Li, Y.; Houghten, R.A.; Martinez-Mayorga, K. The role of imidazole in peptide cyclization by transesterifi-cation: Parallels to the catalytic triads of serine proteases. *Org. Biomol. Chem.* **2013**, *11*, 2979–2987. [CrossRef]

55. Brancolini, G.; Bellucci, L.; Maschio, M.C.; Di Felice, R.; Corni, S. The interaction of peptides and proteins with nanostructures surfaces: A challenge for nanoscience. *Curr. Opin. Colloid Interface Sci.* **2019**, *41*, 86–94. [CrossRef]

56. Brancolini, G.; Tozzini, V. Multiscale modeling of proteins Interaction with functionalized nanoparticles. *Curr. Opin. Colloid Interface Sci.* **2019**, *41*, 66–73. [CrossRef]

57. Brancolini, G.; Lopez, H.; Corni, S.; Tozzini, V. Low-Resolution Models for the Interaction Dynamics of Coated Gold Nanoparticles with beta2-microglobulin. *Int. J. Mol. Sci.* **2019**, *20*, 3866. [CrossRef] [PubMed]

58. Dutta, S.; Bellucci, L.; Agostini, M.; Gagliardi, M.; Corni, S.; Cecchini, M.; Brancolini, G. Atomistic simulations of gold surface functionalization for nanoscale biosensors applications. *Nanotechnology* **2020**, *32*, 095702. [CrossRef] [PubMed]

59. Iori, F.; Di Felice, R.; Molinari, E.; Corni, S. GolP: An atomistic force-field to describe the interaction of proteins with Au(111) surfaces in water. *J. Comput. Chem.* **2009**, *30*, 1465–1476. [CrossRef]

60. Jorgensen, W.L.; Maxwell, D.S.; Tirado-Rives, J. Development and testing of the OPLS all-atom force field on conforma-tional energetics and properties of organic liquids. *J. Am. Chem. Soc.* **1996**, *118*, 11225–11236. [CrossRef]

61. Brancolini, G.; Toroz, D.; Corni, S. Can small hydrophobic gold nanoparticles inhibit β_2-microglobulin fibrillation? *Nanoscale* **2014**, *6*, 7903–7911. [CrossRef]

62. Cantarutti, C.; Raimondi, S.; Brancolini, G.; Corazza, A.; Giorgetti, S.; Ballico, M.; Zanini, S.; Palmisano, G.; Bertoncin, P.; Marchese, L.; et al. Citrate-stabilized gold nanoparti-cles hinder fibrillogenesis of a pathological variant of β_2-microglobulin. *Nanoscale* **2017**, *9*, 3941–3951. [CrossRef]

63. Brancolini, G.; Maschio, M.C.; Cantarutti, C.; Corazza, A.; Fogolari, F.; Bellotti, V.; Corni, S.; Esposito, G. Citrate stabilized gold nanoparticles interfere with amyloid fibril formation: D76N and DeltaN6 β_2-microglobulin variants. *Nanoscale* **2018**, *10*, 4793–4806. [CrossRef]

64. Brancolini, G.; Kokh, D.B.; Calzolai, L.; Wade, R.C.; Corni, S. Docking of ubiquitin to gold nanoparticles. *ACS Nano* **2012**, *6*, 9863–9878. [CrossRef] [PubMed]

65. Pronk, S.; Pall, S.; Schulz, R.; Larsson, P.; Bjelkmar, P.; Apostolov, R.; Shirts, M.R.; Smith, J.C.; Kasson, P.M.; van der Spoel, D.; et al. GROMACS 4.5: A high-throughput and highly parallel open source molecular simulation toolkit. *Bioinformatics* **2013**, *29*, 845–854. [CrossRef]

66. Guex, N.; Peitsch, M.C. SWISS-MODEL and the Swiss-PdbViewer: An environment for comparative protein modeling. *Electrophoresis* **1997**, *18*, 2714–2723. [CrossRef]

67. Mark, P.; Nilsson, L. Structure and dynamics of the TIP3P, SPC, and SPC/E water models at 298 K. *J. Phys. Chem. B* **2001**, *105*, 24a. [CrossRef]

68. Van Der Spoel, D.; Lindahl, E.; Hess, B.; Groenhof, G.; Mark, A.E.; Berendsen, H.J. GROMACS: Fast, flexible, and free. *J. Comput. Chem.* **2005**, *26*, 1701–1718. [CrossRef] [PubMed]

69. Mcsherry, T.M. General Steepest Descent Algorithm. *IEEE Trans. Aerosp. Electron. Syst.* **1976**, *12*, 12–22. [CrossRef]

70. Bussi, G.; Donadio, D.; Parrinello, M. Canonical sampling through velocity rescaling. *J. Chem. Phys.* **2007**, *126*, 014101. [CrossRef] [PubMed]

71. Parrinello, M.; Rahman, A. Polymorphic transitions in single crystals: A new molecular dynamics method. *J. Appl. Phys.* **1981**, *52*, 7182–7190. [CrossRef]

72. Essmann, U.; Perera, L.; Berkowitz, M.L.; Darden, T.; Lee, H.; Pedersen, L.G. A smooth particle mesh Ewald method. *J. Chem. Phys.* **1995**, *103*, 8577–8593. [CrossRef]

73. Franco-Ulloa, S.; Riccardi, L.; Rimembrana, F.; Pini, M.; De Vivo, M. NanoModeler: A Webserver for Molecular Simulations and Engineering of Nanoparticles. *J. Chem. Theory Comput.* **2019**, *15*, 2022–2032. [CrossRef] [PubMed]

74. Pohjolainen, E.; Chen, X.; Malola, S.; Groenhof, G.; Häkkinen, H. A Unified AMBER-Compatible Molecular Mechanics Force Field for Thiolate-Protected Gold Nanoclusters. *J. Chem. Theory Comput.* **2016**, *12*, 1342–1350. [CrossRef]

75. Heinz, H.; Vaia, R.A.; Farmer, B.L.; Naik, R.R. Accurate Simulation of Surfaces and Interfaces of Face-Centered Cubic Metals Using 12−6 and 9−6 Lennard-Jones Potentials. *J. Phys. Chem. C* **2008**, *112*, 17281–17290. [CrossRef]

76. Lundborg, M.; Lindahl, E. Automatic GROMACS Topology Generation and Comparisons of Force Fields for Solvation Free Energy Calculations. *J. Phys. Chem. B* **2015**, *119*, 810–823. [CrossRef] [PubMed]

77. Bayly, C.I.; Cieplak, P.; Cornell, W.; Kollman, P.A. A well-behaved electrostatic potential based method using charge restraints for deriving atomic charges: The RESP model. *J. Phys. Chem.* **1993**, *97*, 10269–10280. [CrossRef]

78. Vanquelef, E.; Simon, S.; Marquant, G.; Garcia, E.; Klimerak, G.; Delepine, J.C.; Cieplak, P.; Dupradeau, F.-Y. R.E.D. Server: A web service for deriving RESP and ESP charges and building force field libraries for new molecules and molecular fragments. *Nucleic Acids Res.* **2011**, *39*, W511–W517. [CrossRef] [PubMed]

79. Vanzan, M.; Rosa, M.; Corni, S. Atomistic insight into the aggregation of [Au25(SR)18]q nanoclusters. *Nanoscale Adv.* **2020**, *2*, 2842–2852. [CrossRef]

80. Evans, D.J.; Holian, B.L. The Nose–Hoover thermostat. *J. Chem. Phys.* **1985**, *83*, 4069. [CrossRef]

81. Heikkilä, E.; Gurtovenko, A.A.; Martinez-Seara, H.; Häkkinen, H.; Vattulainen, I.; Akola, J. Atomistic Simulations of Functional Au144(SR)60 Gold Nanoparticles in Aqueous Environment. *J. Phys. Chem. C* **2012**, *116*, 9805–9815. [CrossRef]

82. Gabdoulline, R.; Wade, R. Simulation of the diffusional association of barnase and barstar. *Biophys. J.* **1997**, *72*, 1917–1929. [CrossRef]

83. Baker, N.A.; Sept, D.; Joseph, S.; Holst, M.J.; McCammon, J.A. Electrostatics of nanosystems: Application to microtu-bules and the ribosome. *Proc. Natl. Acad. Sci. USA* **2001**, *98*, 10037–10041. [CrossRef] [PubMed]

84. Ortega, A.; Amoros, D.; Garcia de la Torre, J. Prediction of hydrodynamic and other solution properties of rigid pro-teins from atomic- and residue-level models. *Biophys. J.* **2011**, *101*, 892–898. [CrossRef] [PubMed]

85. Grell, L.; Parkin, C.; Slatest, L.; Craig, P.A. EZ-Viz, a tool for simplifying molecular viewing in PyMOL. *Biochem. Mol. Biol. Educ.* **2006**, *34*, 402–407. [CrossRef] [PubMed]